Featured in Physics

Resource-Efficient Cross-Platform Verification with Modular Superconducting Devices

Kieran Dalton,[1,2,3,*] Johannes Knörzer,[1,2] Finn Hoehne,[1] Yongxin Song,[1,2,3] Alexander Flasby,[1,3] Dante Colao Zanuz,[1,2] Mohsen Bahrami Panah,[1,3] Ilya Besedin,[1,2,3] Jean-Claude Besse,[1,2,3] and Andreas Wallraff[1,2,3,†]

[1] *Department of Physics, ETH Zürich, CH-8093 Zurich, Switzerland*
[2] *Quantum Center, ETH Zürich, CH-8093 Zurich, Switzerland*
[3] *ETH Zürich—PSI Quantum Computing Hub, Paul Scherrer Institut, CH-5232 Villigen, Switzerland*

(Received 29 July 2025; revised 7 October 2025; accepted 3 November 2025; published 16 December 2025)

Large-scale quantum computers are expected to benefit from modular architectures. Validating the capabilities of modular devices requires benchmarking strategies that assess performance within and between modules. In this work, we evaluate cross-platform verification protocols, which are critical for quantifying how accurately different modules prepare the same quantum state—a key requirement for modular scalability and system-wide consistency. We demonstrate these algorithms using a six-qubit flip-chip superconducting quantum device consisting of two 3-qubit modules on a single carrier chip, with connectivity for intra- and intermodule entanglement. We examine how the resource requirements of protocols relying solely on classical communication between modules scale exponentially with qubit number, and demonstrate that introducing an intermodule two-qubit gate enables subexponential scaling in cross-platform verification. This approach reduces the number of repetitions required by a factor of 4 for three-qubit states, with greater reductions projected for larger and higher-fidelity devices.

DOI: 10.1103/czph-xpzs

I. INTRODUCTION

The advent of quantum computation promises to accelerate the simulation of complex quantum systems and is expected to access a strictly larger complexity class of problems than those efficiently addressable with conventional computation [1–3]. To achieve this goal, we require devices containing thousands of qubits capable of applying millions of gates at sufficiently low error rates, with additional qubit-number overhead from quantum error correction [4–7]. To reach this scale within practical constraints, it may be necessary to use modular devices consisting of multiple independent quantum processors linked with quantum channels [8,9]. In the case of superconducting qubits, this modularity may be achieved between different modules in the same package [10–12], different packages in the same cryostat [13,14], and even different cryostats, either with native microwave interconnects [15,16] or transduction and optical interconnects [17–21].

As modular devices scale to larger qubit numbers, benchmarking techniques must also scale efficiently to remain practical. Existing strategies typically fall into two categories: component-level benchmarking, which assesses the performance of individual operations such as single- and two-qubit gates [22–25], and holistic benchmarking, which evaluates the behavior of an entire device using metrics such as quantum volume [26] or mirror-circuit fidelity [27]. While component-level approaches require extensive testing across all subsystems, holistic benchmarks often depend on classical simulation for result verification—a step that becomes computationally prohibitive as system size increases [25,28]. This scalability constraint highlights the need for verification protocols that are both experimentally feasible and capable of capturing full-system performance in large modular architectures.

A promising approach to scalable end-to-end benchmarking is cross-platform verification via distributed inner-product estimation [29–32]. Here, one prepares a quantum state on one subsystem, that may be the result

*Contact author: kieran.dalton@phys.ethz.ch
†Contact author: andreas.wallraff@phys.ethz.ch

Published by the American Physical Society under the terms of the Creative Commons Attribution 4.0 International license. Further distribution of this work must maintain attribution to the author(s) and the published article's title, journal citation, and DOI.

of a computation, and then estimates the inner product between this state and a nominally identical state prepared on another subsystem. In practice, gate errors and decoherence introduce imperfections that lead to differences in the prepared states. Quantifying how much the nominally identical states deviate, with the help of inner-product estimation, can be a useful diagnostic tool. For states with low magic (i.e., flat Pauli distributions) and low entanglement, this estimation can be carried out efficiently using only local operations and classical communication (LOCC) between the modules [33]. However, for arbitrary mixed states, the number of repetitions required without coherent two-copy access and under LOCC scales exponentially with system size [30,34]. This limitation is lifted when modules are connected through high-fidelity quantum links, as will be necessary for executing quantum algorithms distributed over different modules. In this setting, coherent access to a second imperfect copy of a quantum state, especially if it is too large to fully characterize through quantum state tomography, becomes a powerful resource that enables sample-efficient comparison of large-scale quantum processing units through protocols such as the SWAP test or Bell-basis measurements (BBMs) [35–38].

Previous experimental work on cross-platform verification has focused exclusively on the LOCC variant, for both ion traps [29] and superconducting circuits [39], and between ion traps and superconducting circuits [40,41]. While two-copy measurements have been used to extract information about entanglement in atomic systems [42–44], to date, no experiments have demonstrated distributed inner-product estimation using quantum communication between separate modules. In this work, we evaluate different cross-platform verification protocols using our six-qubit modular superconducting device, consisting of two modules each containing three qubits on the same carrier chip. This modular device acts as a proof of concept for future large-scale modular devices, which will provably benefit from entangled measurements across quantum states in situations in which the individual states are too large to be fully characterized. We benchmark the performance of this device, and use it to compare the relative performance of protocols using LOCC and protocols which make use of the quantum links between the modules. To compare these protocols, we use them to estimate the inner product between one-, two- and three-qubit states on each module, then compare these estimated inner products. We additionally consider the resource scaling, with the state dimension, required to estimate the inner product to a given statistical variance using different protocols. To extend the scaling analysis of required experimental runs to larger systems, we also perform numerical simulations on four- and five-qubit modules. The results thereby obtained give us additional confidence that our projected scaling improvements will hold under a realistic error model.

II. DEVICE DESIGN AND PERFORMANCE

As superconducting quantum devices increase in scale, they face limitations in routing, crosstalk [45,46] and fabrication yield [47]. To alleviate these limitations, the largest devices use three-dimensional- (3D) integration technologies such as flip-chip bonding [48–50]. Here, device components are distributed across the opposing faces of two vertically stacked chips. Modular devices promise to further improve device performance and fabrication yield using more than two chips [9]. In this work, we consider a modular device composed of multiple smaller upper chips, the modules, bonded to a single larger lower chip, the carrier.

Recent realizations of modular devices have focused on implementing two-qubit gates between qubits on different modules [10–12,51,52]. Building upon the intermodule two-qubit gate of Ref. [51], we present a superconducting device consisting of six flux-tunable qubits divided between two three-qubit modules on a single carrier chip. The qubits are coupled (with fixed interaction strength) in a two-by-three ladder topology, with both intermodule and intramodule two-qubit gates implemented using nanosecond-timescale qubit frequency control with individual qubit flux lines [53–55]. See Ref. [51] for a more detailed discussion of the two-qubit gate design. We present the measured device parameters in Appendix A, and the measurement apparatus in Appendix B.

Each set of three qubits is read out using a frequency-multiplexed feedline coupled to individual Purcell filters attached to the readout resonator of each qubit [56,57]. All readout circuitry and control lines are routed on the bottom carrier chip. When two lines must cross, one line is routed through indium bumps via the opposite chip. The two 5.8 mm by 12 mm modules are flip-chip bonded to the 14.3 mm by 14.3 mm carrier [see the conceptual sketch in Fig. 1(a) and the photograph of the assembled device in Fig. 1(b)]. Further design considerations, and the device fabrication procedure, are described in Refs. [51,58].

We characterize the device performance by benchmarking readout and single- and two-qubit gates. For qubit (qutrit) single-shot readout, we measure a median assignment error of 1.01 % (2.21 %), with a range 0.80–1.43 % (1.77–3.45 %). For all measurements, we use single-shot readout both at the start and end of the circuit, with a preselection pulse to discard cases in which residual excitation errors are detected, heralding the qubit ground state. This rejects 0.78 % (0.24–2.76 %) of preparations per qubit. When preparing a three-qubit state, we obtain a total rejected fraction due to preselection of 1.7 % (1.8 %) on the left (right) module, with differences from the individual qubit characterization due to fluctuating qubit relaxation

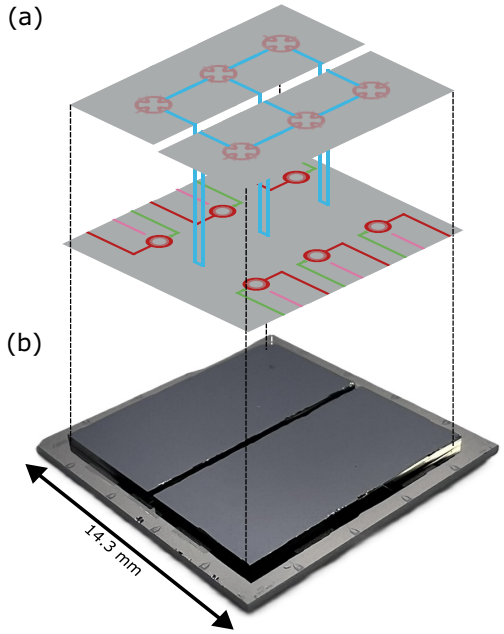


FIG. 1. (a) A schematic of the device design, showing the top modules and bottom carrier, with the qubit island (gaps where metal is removed are colored light red), qubit-qubit coupler (light blue), readout coupling pad (red), flux line (green), charge line (pink), and ground plane (gray). The vertical separation between the chips is 10 μm. (b) A photograph of the assembled device.

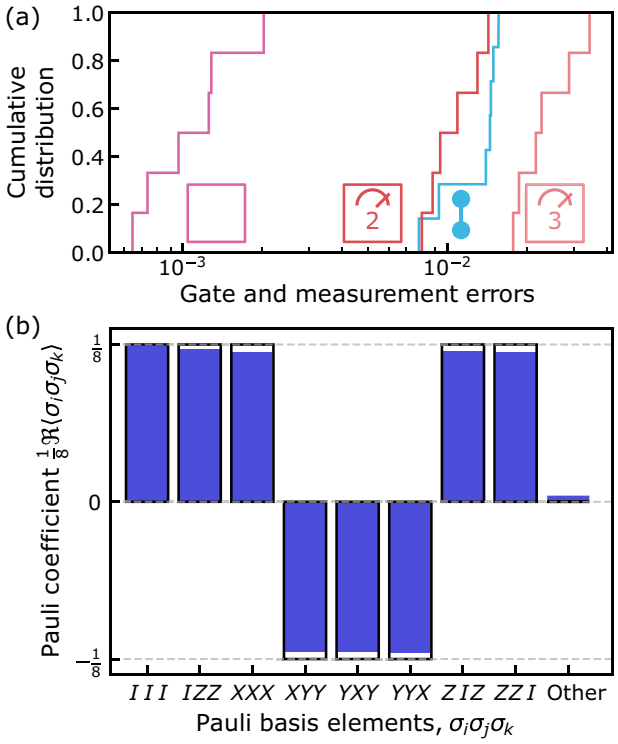


FIG. 2. (a) The empirical cumulative distribution function of device errors, with the error rates of single-qubit gates (pink square), two-qubit gates (double cyan circles), and readout in the qubit and qutrit manifold (red measurement icons). (b) The state-tomography result for a three-qubit GHZ state prepared on the three qubits of the left module. We show Pauli decomposition coefficients which are expected to be nonzero. Ideal results in the absence of noise are represented by the black-outlined bars. The remaining coefficient with the largest absolute value is presented as "Other".

times (see Appendix A). We benchmark single-qubit gates using randomized benchmarking [23], obtaining a median single-qubit error rate of 0.11 % (0.06–0.20 %). Similarly, interleaved randomized benchmarking [22] provides a median two-qubit error rate of 1.45 % (0.78–1.56 %). These are comparable to error rates achieved in similar planar [59,60] and 3D-integrated [11,51,61] devices. However, the two-qubit gate fidelities are lower than those in large 3D-integrated devices using tunable couplers [48–50]. See Ref. [51] for a more detailed discussion of the performance of a two-qubit gate with an identical design. For all experiments, following data acquisition, we postselect to remove the repetitions where qubits are detected in the second excited state. We measure the population leakage rates for individual two-qubit gates and three-qubit state preparation to quantify this postselected fraction. We measure a median population leakage into the second excited state of 0.21 % (0.10–0.52 %) per two-qubit gate. This leakage is included in the aforementioned two-qubit error rates. When preparing a three-qubit state with two entangling gates, we obtain a total postselected fraction due to leakage of 0.49 % (0.70 %) on the left (right) module. Given that these postselected fractions are small, we do not use constructive interference for leakage calibration [62] or leakage-reduction pulses [63,64]. These techniques, or other techniques to reduce leakage, will be necessary in the future for experiments involving more qubits and deeper circuits. We present the error rates for all qubits and two-qubit gates in a cumulative distribution plot, shown in Fig. 2(a).

To carry out a holistic assessment of device performance, we prepare a maximally entangled three-qubit Greenberger-Horne-Zeilinger (GHZ) state on each three-qubit module. We use quantum state tomography with maximum-likelihood estimation [65] to find the most likely physical density matrix of the state. This involves measuring the state in an over-complete basis set of single-qubit Pauli bases (i.e., X, Y and Z bases) and their negatives $-X$, $-Y$ and $-Z$. This allows us to correct for systematic errors in measurement axis rotations and detection bias [66]. Additionally, we use calibration measurements of all qubits in their computational basis states for readout-error correction [67].

The resulting three-qubit states have measured fidelities [according to Eq. (1)] of 96.3(1) % and 95.1(1) %. Here, the uncertainties are estimated using bootstrapping. We simulate the state-preparation circuit (the gray part

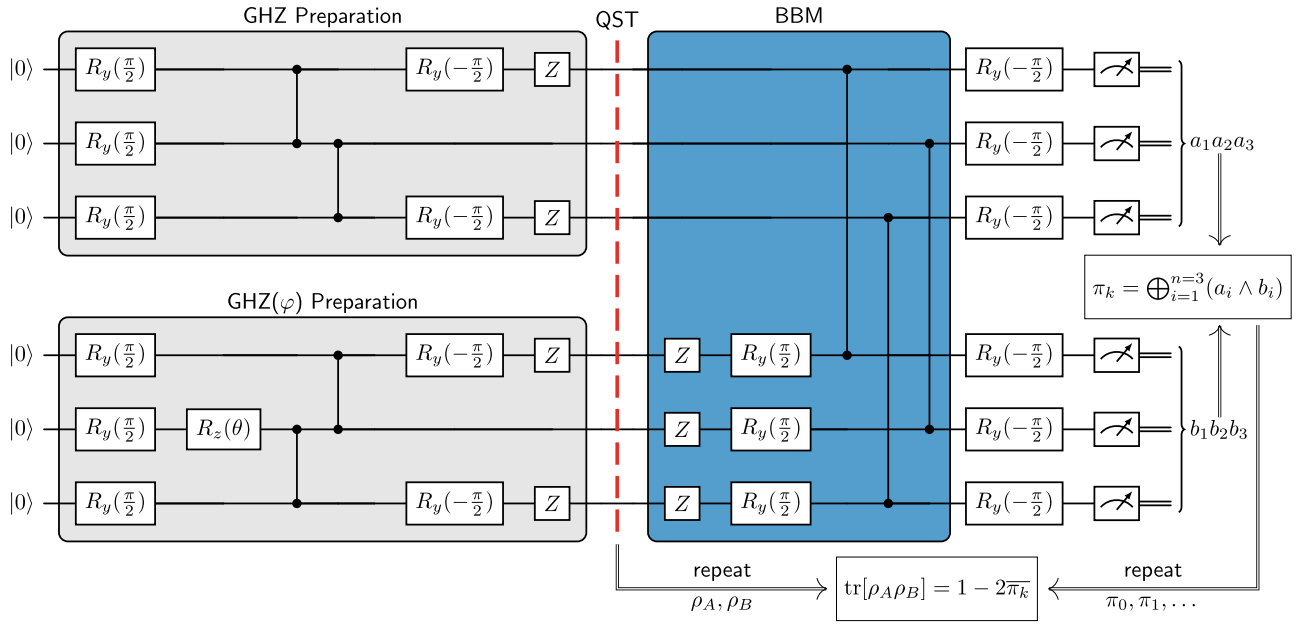


FIG. 3. The circuit diagram for the GHZ state preparation and the Bell-basis measurement (BBM) protocol. Measuring corresponding qubits on each module in the Bell basis results in two bit strings a_i and b_i. Analyzing these as described in the text results in an estimate of the inner product between the states on each module. The red dotted line indicates where the quantum state tomography (QST) circuit would conclude, with measurements in a complete basis set.

of Fig. 3) using a realistic error model which takes into account the measured median error rates and relaxation times (see Appendix C). The simulated fidelity is 95.8 %, consistent with the measured fidelities. The infidelity is dominated by two-qubit gate errors. The Pauli-basis decomposition of the resulting density matrix is presented in Fig. 2(b) for the left module shown in Figs. 1(a) and 1(b).

III. DISTRIBUTED INNER-PRODUCT ESTIMATION

A. Quantum state tomography

Distributed inner-product estimation is widely recognized as an important method for benchmarking near-term quantum computers [25,28–30,40,68]. The task of distributed inner-product estimation is to infer the inner product, $\mathrm{tr}(\rho_A\rho_B)$, between two spatially separated quantum states ρ_A and ρ_B with the same Hilbert-space dimension, which are hosted in two different modules A and B. If the state purities are also known, knowledge of the inner product allows the state fidelity,

$$\mathcal{F}(\rho_A, \rho_B) = \frac{\mathrm{tr}(\rho_A\rho_B)}{\max\{\mathrm{tr}(\rho_A^2), \mathrm{tr}(\rho_B^2)\}}, \tag{1}$$

to be calculated [69]. If either state is pure, i.e., if $\mathrm{tr}(\rho_A^2) = 1$ or $\mathrm{tr}(\rho_B^2) = 1$, the inner product in the numerator coincides with the state fidelity. We note that this is one of several operationally meaningful definitions of quantum state fidelity, and in particular one that fulfills desirable mathematical properties and is upper bounded by the more commonly known Uhlmann-Jozsa fidelity, for arbitrary density matrices [70]. In contrast to the latter, the fidelity in Eq. (1) is usually more straightforward to calculate. Even more importantly, it is of particular interest in the context of cross-platform verification, as it can be obtained from randomized measurements [29] and its numerator can be estimated using two-copy measurements [31], as will be discussed later.

To benchmark the performance of both three-qubit modules, we initially prepare the phase-shifted n-qubit GHZ state on each module, defined as

$$|\mathrm{GHZ}\rangle_n^{(\varphi)} = \frac{1}{\sqrt{2}}\left(|0\rangle^{\otimes n} + e^{i\varphi}\,|1\rangle^{\otimes n}\right), \tag{2}$$

where $n \in \{1, 2, 3\}$. On one of the modules, we prepare a GHZ state with $\varphi = 0$. On the other, we apply a variable phase φ to the prepared state, as described with a conceptual circuit for $n = 3$ in the gray region of Fig. 3. We vary this phase to test both nominally identical and nominally orthogonal states. In our implementation of this circuit, we take advantage of virtual-Z gates [71]. This results in the separable $2n$-qubit state $|\mathrm{GHZ}\rangle_n^{(0)} \otimes |\mathrm{GHZ}\rangle_n^{(\varphi)}$.

We carry out n-qubit quantum state tomography to estimate the density matrix for the single-module n-qubit subsystem $|\mathrm{GHZ}\rangle_n^{(0)}$. We then repeat this on the other module to find the density matrix of the n-qubit subsystem $|\mathrm{GHZ}\rangle_n^{(\varphi)}$, for 15 equally spaced values of $\varphi \in [0, 2\pi]$.

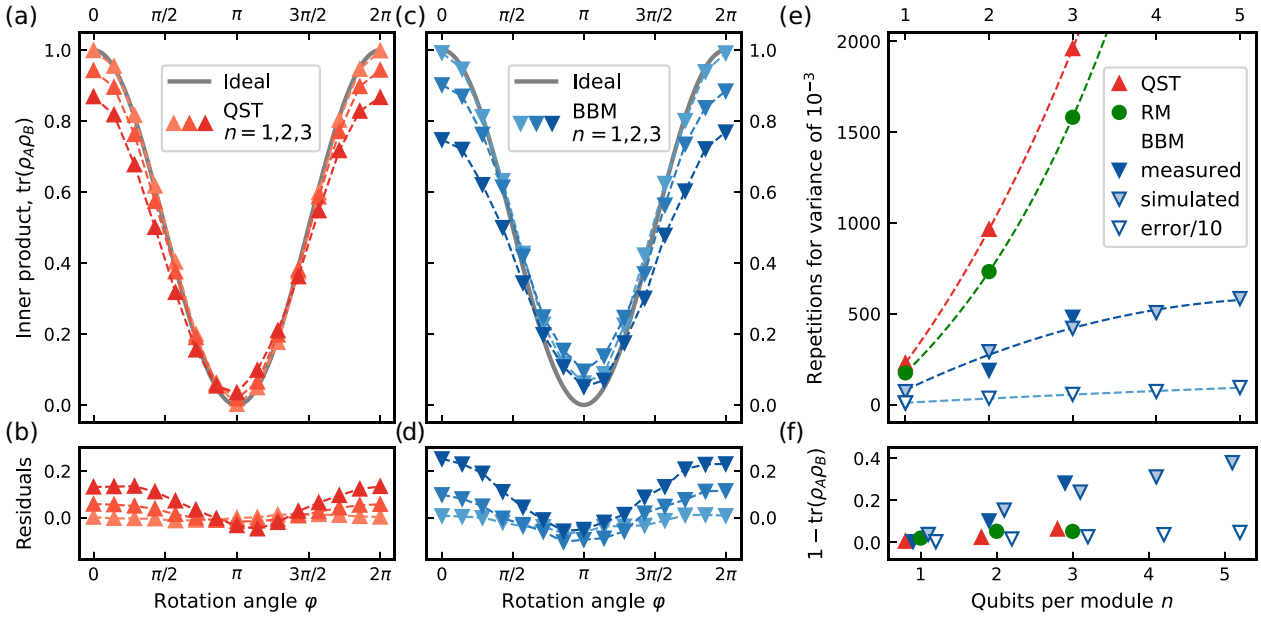


FIG. 4. (a)–(d) Measured and calculated inner products for two n-qubit states, $\frac{1}{\sqrt{2}}\left(|0\rangle^{\otimes n}+|1\rangle^{\otimes n}\right)$ and $\frac{1}{\sqrt{2}}\left(|0\rangle^{\otimes n}+e^{i\varphi}|1\rangle^{\otimes n}\right)$, prepared on the left and right modules, respectively. The overlap is calculated using quantum state tomography (QST, red symbols) and Bell-basis measurements (BBMs, blue symbols). The statistical error bars are smaller than the symbol sizes. (e) The number of measurements needed to estimate the inner product between two identically prepared $|\mathrm{GHZ}\rangle_n^{(0)}$ states to a statistical variance of 10^{-3}. The variance is calculated by taking 100 samples of varying size, with replacement, from a large data set. The relationship between variance and the sample size is then interpolated for the y-axis values. For both plots, simulated data for the Bell-basis measurement protocol, using the median errors presented in Fig. 2(a), are presented as light blue downward triangles. White downward triangles represent simulations with all error rates divided by ten. Exponential (for quantum state tomography and randomized measurements) and quadratic (for Bell-basis measurements) fitted curves are provided as dashed lines as a guide to the eye. The statistical error bars are smaller than the symbol sizes. (f) The measured inner product for identically prepared $|\mathrm{GHZ}\rangle_n^{(0)}$ states using Bell-basis measurements, quantum state tomography, and randomized measurements (RMs).

While only one GHZ state on one module is characterized, the full $2n$-qubit state is always prepared. This ensures that any intermodule crosstalk or spectator errors [72] due to the operations on one module affect the state characterized on the other module. For each quantum state tomography repetition, each set of bases and calibration points is measured 10^4 times.

We then calculate the inner product between the zero-phase state on the first module and each state of a given φ prepared on the second module. For $n \in \{1,2,3\}$, the estimated inner product shows qualitative agreement with the calculated value of $\mathcal{F}(\rho_n^0, \rho_n^\varphi) = (1+\cos\varphi)/2$, where $\rho_n^\varphi = |\mathrm{GHZ}\rangle_n^{(\varphi)}\langle\mathrm{GHZ}|_n^{(\varphi)}$ [see Figs. 4(a) and 4(b)]. We observe near-unity inner product for identically prepared states, and near-zero overlap for states with opposite phase. The peak measured inner products are lower for greater numbers of qubits, as one would expect from deeper state-preparation circuits.

B. Bell-basis measurements

If quantum information can be shared among the modules A and B, it is possible to perform a SWAP test [35] or Bell-basis measurements [37,38] between them to carry out distributed inner-product estimation. Bell-basis measurements consist of pairwise two-qubit measurements in the Bell basis between corresponding qubits on each module. Although Bell-basis measurements involve additional classical postprocessing, they do not require an ancilla qubit, as the SWAP test does.

We now compare the inner products measured using quantum state tomography to those estimated with Bell-basis measurements. In a separate measurement run, we prepare the same separable $2n$-qubit state, $|\mathrm{GHZ}\rangle_n^{(0)} \otimes |\mathrm{GHZ}\rangle_n^{(\varphi)}$, and then apply the Bell-basis measurement circuit presented in the blue-shaded region of Fig. 3.

Measuring all $2n$ qubits, one parametrized by φ and one with $\varphi = 0$, results in two bit strings of length n: a_i and b_i. The parity of the bit string resulting from the bit-wise AND operator ($\wedge$) between the two bit strings is calculated, $\pi_k = \bigoplus_{i=1}^{n}(a_i \wedge b_i)$. The mean value of this parity, over many repetitions, determines the inner product, $\mathrm{tr}(\rho_A\rho_B) = 1 - 2\overline{\pi_k}$. We repeat the algorithm for the same 15 values of φ, 10^4 times each.

For Bell-basis measurements, we again observe qualitative agreement with the calculation, with trace overlap less

than 0.1 for nominally orthogonal states and greater than 0.7 for nominally identical states, qualitatively the same behavior as for quantum state tomography [see Figs. 4(c) and 4(d)]. The deviation from theory is greatest (above 0.25 for $n = 3$) for nominally identical states with an expected trace overlap of one, and also high (above 0.05 for $n = 3$) for nominally orthogonal states with zero expected trace overlap. This is because noise reduces the purity of the prepared GHZ states by degrading the coherent superpositions between $|0\rangle^{\otimes n}$ and $|1\rangle^{\otimes n}$. By reducing state purity, the trace overlap $\mathrm{tr}(\rho_A \rho_B)$ for nominally identical states is suppressed. Similarly, for nominally orthogonal states, noise enhances the trace overlap, as the different states tend toward the same maximally mixed state (in the case of simple depolarizing noise).

The inner-product contrast is lower for the Bell-basis measurement data than for the quantum state tomography data, mainly due to the additional two-qubit gates required by the Bell-basis measurement protocol. Additionally, the reliance of the Bell-basis measurement protocol on bit-string parity makes it more sensitive to readout misclassification errors. We expand on this further with an error-budget analysis in Appendix C. This error-budget analysis relies on noisy simulations of the experiment which have good quantitative agreement with the measured data. We present the measured inner products of Figs. 4(c) and 4(d) alongside the simulated inner products in Figs. 7(c)–7(e) in Appendix E, and the figures display good quantitative agreement between them. Using prior measurements of a readout assignment matrix, the Bell-basis measurement data can be readout-error corrected. This reduces the maximal deviation from theory to 0.17 for $n = 3$, closer to the quantum state tomography value of 0.13. Due to the additional measurements required, and device performance variations (see Appendix A), we have not readout-error corrected the Bell-basis measurement data in Figs. 4(c) and 4(d).

IV. SAMPLING-COMPLEXITY ANALYSIS

We now examine the relative scaling, with Hilbert-space dimension, of the number of repetitions required for distributed inner-product estimation, with and without quantum communication between the modules. We record a large data set of 10^4 repetitions (for each basis) for quantum state tomography and 1.5×10^5 repetitions for Bell-basis measurements, and calculate the inner products of two identically prepared $|\mathrm{GHZ}\rangle_n^{(0)}$ states (for $n = 1, 2, 3$) using both methods.

Quantum state tomography, particularly involving an over-complete basis set, is inefficient for distributed inner-product estimation and thus not scalable to large system sizes [30]. As a more efficient method, we use the same data set to estimate the inner product using randomized measurements and classical correlations [29,73], selecting 3^n measurement bases using the greedy algorithm presented in Appendix D. We choose 3^n measurement settings as a balance between sample efficiency and the variance of the resulting inner product. Previous experimental demonstrations of cross-platform verification in ion-trap and superconducting devices have used this randomized-measurement approach [40,73].

We estimate the variance of the inner product for a given number of repetitions using bootstrapping. Specifically, we draw N_p repetitions from the data set 100 times, sampling with replacement so that repetitions may appear multiple times. For quantum state tomography, each selected repetition includes all measured bases. We calculate the inner product for each of the 100 subsamples of size N_p, and determine the variance of these values. For randomized measurements, we perform a new basis selection for each subsample.

We repeat this procedure for multiple subsample sizes N_p and fit the resulting variances to a power law. An example data set is provided in Fig. 7(b) in Appendix E. This fit allows us to determine the number of measurements required to reach a given target variance, which we choose to be 10^{-3}. We choose this value such that the statistical variations are lower than the systematic reductions of inner product due to noise, which are all greater than 10^{-2}. This method allows us to compare all three protocols on an even footing.

For LOCC-based methods (quantum state tomography and randomized measurements), we see the number of necessary repetitions rise quickly with system size, reaching over 1500 for three-qubit states. The data agree well with an exponential fit to the measured quantum state tomography (red triangles) and randomized measurements (green circles) data [see the dashed lines in Fig. 4(e)]. This aligns with theory: estimating the inner product $\mathrm{tr}(\rho_A \rho_B)$ using LOCC requires an exponential number of measurements [30]. If one first tomographically reconstructs both ρ_A and ρ_B to compute $\mathrm{tr}(\rho_A \rho_B)$, it is evident that the exponential scaling of resources is inherited from quantum state tomography [74], which is currently practically limited to approximately ten-qubit states [75]. Since only three system sizes are measured, the empirical range over which this scaling can be observed is limited.

Bell-basis measurements, on the other hand, require significantly fewer repetitions for all n. For $n = 3$, Bell-basis measurements require four times fewer repetitions than quantum state tomography for inner-product estimation with a variance of 10^{-3} [see the dark blue triangles in Fig. 4(e)]. However, the measured scaling for Bell-basis measurements is not constant with the number of qubits, as expected theoretically in the absence of noise [31]. This can be explained by considering the increase in error rates with system dimension. As the number of qubits is increased, the measured inner product decreases, and hence the probability of an even-parity bit string in

Bell-basis measurement analysis also decreases (provided that the inner product exceeds 0.5). Considering each experimental repetition as a Bernoulli trial with a success probability close to unity, one would expect a linear increase in variance for a fixed number of repetitions, with a quadratic contribution for trace overlaps further from unity.

We emphasize that the improved scaling of Bell-basis measurements must be considered alongside its additional hardware requirements, particularly when the two-qubit gates in the Bell-basis measurements cannot be executed in a single parallel operation. To assess these hardware requirements further, we simulate the Bell-basis measurement protocol using a symmetric depolarizing error channel with the median gate and readout error rates presented in Fig. 2(a). We provide further details of these simulations in Appendix C. Performing the same analysis as for the experimental data, the simulated data agree quantitatively with the measurements, indicating a faithful simulation. These simulated data are represented by the light blue downward triangles in Figs. 4(e) and 4(f). Reducing all error rates by a factor of 10, our simulated data approach the expected constant scaling without noise, with near-unity trace overlaps [see the white downward triangles in Figs. 4(e) and 4(f)]. We provide a quadratic fit to the simulated Bell-basis measurement data as a guide to the eye. This closely follows the data, and has the theoretically expected negative coefficient for the quadratic term.

We emphasize that the expected exponential scaling complexity for LOCC methods applies to generic arbitrary quantum states. For specific classes of states or with prior knowledge, they can perform significantly better. For instance, efficient tomographic methods are known if ρ is fairly pure [76], permutationally invariant [77] or well approximated by a small matrix-product state [78]. Efficiency can also improve by replacing standard Pauli measurements with alternative bases such as mutually unbiased bases [79] or threshold quantum state tomography [80]. Inner-product estimation similarly benefits from prior knowledge: for many pure target states ρ_A that are known classically, the overlap $\mathrm{tr}(\rho_A\rho_B)$ with a prepared state ρ_B can be estimated with a constant number of measurements [81]. Even when both states are unknown, efficient estimation is possible for states with low magic (i.e., flat Pauli distributions [82]) and low entanglement [33].

V. DISCUSSION AND OUTLOOK

In this work, we have demonstrated efficient cross-platform verification using three intermodule coupling buses between two three-qubit modules on a single carrier chip. We have compared the performance of the sample-efficient Bell-basis measurement protocol [37,38] to methods using only local operations and classical communication (LOCC) between the modules. We have compared them both in terms of the estimated inner product between identically prepared states on each module and the resource scaling with states of different dimension. It is noteworthy that there are other similarity measures between quantum states, such as the trace distance, which can only be efficiently estimated with existing algorithms in specific cases [83,84]. This constitutes an important open research question [85].

We have demonstrated that although the Bell-basis measurement protocol introduces intermodule two-qubit gates that modestly reduce the measured inner product compared to LOCC-based protocols, Bell-basis measurements require substantially fewer repetitions to achieve a fixed statistical precision for states of increasing dimension, in contrast to the exponential resource scaling of trace-overlap estimation based on quantum state tomography [78] and randomized measurements [73]. Despite the small sample size, our data agree well with exponential scaling for LOCC-based protocols, and quadratic scaling for Bell-basis measurements. Notably, to estimate the trace overlap between two nominally identical three-qubit GHZ states to a given variance, Bell-basis measurements require four times fewer repetitions than quantum state tomography. This highlights the utility of quantum communication in distributed quantum architectures. We expect that the improved scaling will become more relevant as modular quantum systems grow in size. Provided that two-qubit gate and readout errors are reduced, this establishes Bell-basis measurements between modules as a valuable tool for the scalable benchmarking of modular quantum devices, a critical requirement as quantum processors grow beyond monolithic architectures.

While we have demonstrated cross-platform verification for three-qubit GHZ states, future studies could explore more general scenarios, such as verifying transformations or channels, which requires adapting Bell-basis measurements to compare unitaries or process matrices rather than states [31]. This, however, comes at a cost. Standard approaches such as Bell-basis measurements or SWAP tests for process fidelity estimation involve averaging over Haar-random input states, which is challenging to implement in practice. In Appendix E, we present a simplified alternative based on sampling input states from the computational basis, which is straightforward to realize experimentally. Although the resulting measure is not a true process fidelity, since it lacks basis independence, it can still serve as a useful performance metric of unitary processes.

Another interesting direction is the study of hybrid verification protocols that combine the strengths of both Bell-basis measurement and LOCC techniques. For example, local operations may serve to diagnose local errors or reduce state space before Bell-basis measurements

are applied [68]. As quantum systems continue to scale, and modular architectures become increasingly prominent, such capabilities will be essential for the reliable certification and operation of distributed quantum processors.

In addition to its utility for cross-platform verification, the ability to perform scalable Bell-basis measurements between separate modules may also prove valuable for Bell-sampling tasks, in which two identical copies of a state are prepared by a quantum circuit and measured in the Bell basis. The measurement results yield information about the underlying quantum state, as they allow us to estimate all 4^n Pauli observables of an n-qubit state highly efficiently [86] and to diagnose circuit errors [87,88].

ACKNOWLEDGMENTS

We thank Graham J. Norris and Christoph Hellings for helpful discussions regarding the experimental setup, and the technical staff at the Quantum Device Laboratory for their support. We thank Andreas Elben for providing feedback on the manuscript, and Johannes Fink for useful discussions regarding optical interconnects and transduction. We acknowledge financial support by the Swiss State Secretariat for Education, Research and Innovation under Contract No. UeM019-11, by the Intelligence Advanced Research Projects Activity (IARPA) and the Army Research Office, under the Entangled Logical Qubits program and Cooperative Agreement No. W911NF-23-2-0212, and by ETH Zurich. The views and conclusions contained in this document are those of the authors and should not be interpreted as representing the official policies, either expressed or implied, of IARPA, the Army Research Office, or the U.S. Government. The U.S. Government is authorized to reproduce and distribute reprints for Government purposes notwithstanding any copyright notation herein.

J.-C.B., J.K., and K.D. planned the experiments. K.D. designed and K.D., A.F., D.C.Z., and M.B.P. fabricated the device. F.H. and K.D. performed all measurements and analyzed all data. I.B. and Y.S. assisted with the experimental setup and measurements. J.K. and K.D. wrote the manuscript with input from all authors. A.W. and J.-C.B. supervised the work.

DATA AVAILABILITY

The data that support the findings of this paper are openly available [89].

APPENDIX A: DEVICE PARAMETERS

Here, we present the device parameters of our six-qubit modular device. We measure the extremal dressed qubit $|g\rangle$-$|e\rangle$ and $|e\rangle$-$|f\rangle$ transition frequencies from Ramsey measurements as a function of the flux bias applied to the qubit, and use these to extract the qubit anharmonicity. These values are presented in the upper half of Table I.

With these parameters, we then extract the qubit charging energy and the qubit Josephson energy by numerically diagonalizing the coupled qubit–resonator–Purcell-filter Hamiltonian, as described in Ref. [51]. These parameters are given in the lower half of Table I.

Qubit relaxation and dephasing times are known to vary over time [90,91]. To characterize this, we perform 20 measurements of the qubit longitudinal-relaxation times (T_1) and transverse-relaxation times (T_2^*) over a period of 25 h. We present the results of these measurements as cumulative distribution functions in Fig. 5. The mean measured T_1 times, in microseconds, for the six qubits on the device are $\{43.0, 62.0, 22.4, 88.3, 24.0, 51.0\}$. The corresponding coefficients of variation (standard deviation divided by mean) are $\{0.20, 0.11, 0.29, 0.15, 0.13, 0.10\}$. For T_2^* times, we measure mean values of $\{40.0, 71.8, 32.6, 88.3, 11.7, 76.5\}$ and coefficients of variation of $\{0.42, 0.36, 0.35, 0.28, 0.21, 0.25\}$. This high degree of variation leads to fluctuations in gate and readout fidelities, and hence state-preparation fidelities. To characterize the effect of these variations, we measure the three-state single-shot readout (SSRO) fidelity and the two-qubit gate fidelity for one pair of qubits, one from each module, repeatedly over 15 h. As with the coherence times, we calculate the coefficient of variation in these fidelities. For the SSRO

TABLE I. The measured and extracted qubit parameters. Measured parameters: the dressed-qubit $|g\rangle$-$|e\rangle$ transition frequency $\omega^{\mathrm{d}}_{\mathrm{q,ge}}(\phi)$ at reduced flux $\phi = \Phi/\Phi_0$ (where Φ is the flux threading the superconducting quantum interference device (SQUID) loop and Φ_0 is the flux quantum) and the qubit anharmonicity $\alpha^{\mathrm{d}}_{\mathrm{f}}(\phi)$. Extracted parameters: the Josephson energy at $\phi = 0$, $E_{\mathrm{J,max}}$ and the charging energy E_{c}. All quantities are expressed in GHz.

		Left-module qubits			Right-module qubits		
Parameter	Unit	1	2	3	4	5	6
$\omega^{\mathrm{d}}_{\mathrm{q,ge}}(0.0)/2\pi$	(GHz)	5.487	5.903	6.364	5.644	5.914	6.450
$\omega^{\mathrm{d}}_{\mathrm{q,ge}}(0.5)/2\pi$	(GHz)	3.757	4.161	4.764	4.088	4.301	4.884
$\alpha^{\mathrm{d}}_{\mathrm{q}}(0.0)/2\pi$	(GHz)	−0.163	−0.150	−0.154	−0.171	−0.161	−0.158
$E_{\mathrm{J,max}}/h$	(GHz)	25.23	30.71	33.92	25.63	29.20	34.64
E_{c}/h	(GHz)	0.160	0.151	0.159	0.166	0.160	0.160

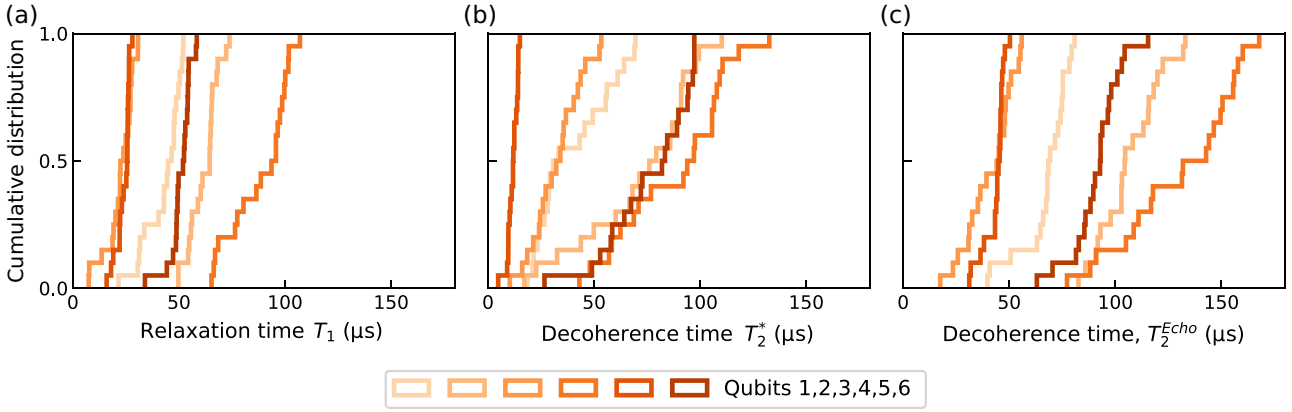


FIG. 5. The cumulative distribution of the qubit coherence times. (a) The qubit longitudinal-relaxation times, T_1. (b) The qubit transverse-relaxation times T_2^*. (c) The qubit transverse-relaxation times with a Hahn-echo pulse, T_2^{echo}.

fidelity, we observe a coefficient of variation of 0.14 for both qubits, consistent with the variation in the T_1 times. For the two-qubit gate fidelity, the calculated coefficient of variation is 0.30, consistent with the variation in the T_2^* times. While these fluctuations will alter the inner products measured using Bell-basis measurements and quantum state tomography, verified using numerical simulation, they are insufficiently large to change the ordering between different protocols, and hence do not change our conclusions.

APPENDIX B: MEASUREMENT APPARATUS

The sample has been measured at the 10 mK stage of a dilution refrigerator, with the shielding configuration described in Ref. [92]. The wiring configuration and room-temperature control electronics are presented in Fig. 6.

For qubit frequency control, we use an *RC* bias tee to combine a static voltage with nanosecond-timescale voltage pulses, determining an external flux through the qubit superconducting quantum interference device (SQUID) loop. The static voltage is generated using a dc source, and the voltage pulses using an arbitrary waveform generator (AWG) with a sampling rate of 2.0 GS/s. The voltage pulses are digitally predistorted to correct for the transfer function of the lines [55].

Qubit *XY* drive pulses are generated by a super-high-frequency qubit controller (SHFQC) using a double-frequency-conversion scheme [93]. Qubit readout is carried out by the SHFQC and a super-high-frequency qubit analyzer (SHFQA), one for each frequency-multiplexed feedline serving each module of three qubits. The readout pulses, generated with a superheterodyne signal generator, pass through the readout feedline, and are then amplified using a near-quantum limited traveling-wave parametric amplifier [94], a high-electron mobility amplifier (HEMT), and a room-temperature low-noise amplifier. For the first feedline (read out using the SHFQC), this amplification chain results in a quantum measurement efficiency [95] of 0.33 for qubit 3.

The SHFQC is triggered using a programmable quantum system controller (PQSC), while the SHFQA is triggered via the AWG.

APPENDIX C: NUMERICAL SIMULATIONS

We simulate the performance of our six-qubit device using the QISKIT software package [96]. A simple symmetric depolarizing channel is applied to the qubits involved in readout, single-qubit and two-qubit gates, using the median error rates discussed in Sec. II, presented in Fig. 2(a). The channel is defined as [3]

$$\rho \mapsto (1-p)\rho + p\frac{I}{2^N}, \tag{C1}$$

with the depolarizing parameter p.

We apply a thermal-relaxation error channel to qubits which are not acted upon by each gate, to account for idling errors, defined as

$$\rho_{11}(t) = \rho_{11}(0)e^{-t/T_1} + p_{\text{th}}(1-e^{-t/T_1}), \tag{C2}$$

$$\rho_{00}(t) = \rho_{00}(0)e^{-t/T_1} + (1-p_{\text{th}})(1-e^{-t/T_1}), \tag{C3}$$

$$\rho_{10}(t) = \rho_{10}(0)e^{-t/T_2}, \tag{C4}$$

$$\rho_{01}(t) = \rho_{01}(0)e^{-t/T_2}, \tag{C5}$$

where T_1 is the mean longitudinal-relaxation time of the qubit, T_2 is the mean transverse-relaxation time, t is the gate time (40 ns for single-qubit and 100 ns for two-qubit gates) and p_{th} is the qubit residual excited-state population. These values are measured in separate characterization experiments.

We simulate the Bell-basis measurement protocol discussed in Sec. III B. We include the effect of noise in

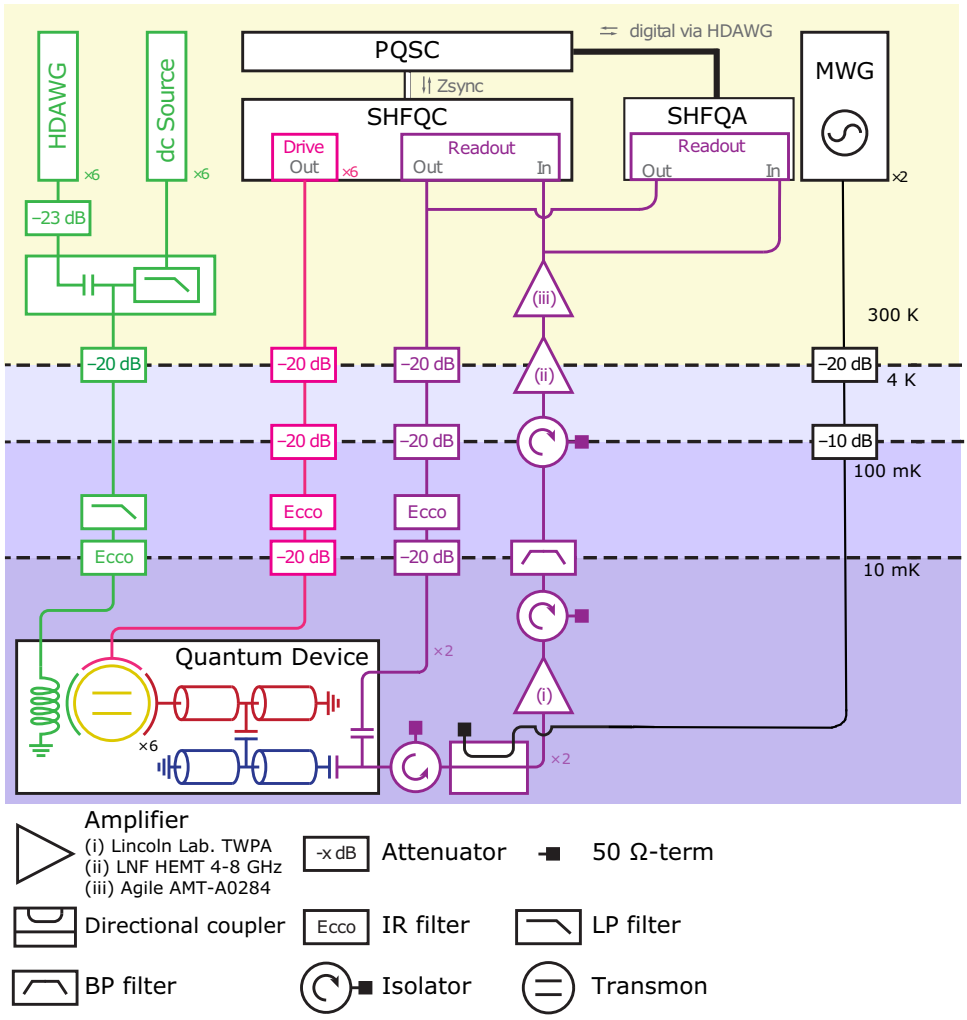


FIG. 6. The measurement-setup wiring diagram. See the text of Sec. B for details. This is exemplary for one qubit and one readout line, and does not display the whole setup.

both the state preparation and the Bell-basis measurement protocol illustrated in Fig. 3.

We observe a cosinusoidal variation in simulated trace overlap, as expected for the states $|\mathrm{GHZ}\rangle_n^{(0)}$ and $|\mathrm{GHZ}\rangle_n^{(\varphi)}$. Simulations involving more qubits and two-qubit gates show reduced contrast in the trace overlap [orange squares in Figs. 7(c)–7(e) in Appendix E]. These data are in quantitative agreement with the Bell-basis measurement data (blue triangles). A validated simulation allows us to extract an error budget for our Bell-basis measurement protocol, including the errors which occur during single-qubit gates, two-qubit gates, and readout.

To do this, we apply the method presented in Ref. [97]. We simulate the Bell-basis measurement protocol for two identical $|\mathrm{GHZ}\rangle_n^{(0)}$ states, using the measured median error rates. We then halve each error rate in turn (including halving the gate times, to reduce idling error), allowing the partial derivative of the total error rate with respect to each error source to be estimated:

$$\frac{\partial E(p_i)}{\partial p_i} \approx \frac{E(p_i) - E\left(\frac{p_i}{2}\right)}{p_i - \frac{p_i}{2}}, \tag{C6}$$

where $E = 1 - \mathrm{tr}(\rho_A \rho_B)$. This partial derivative defines a weight. One can then find the product of this weight with the measured median error rate of that error source, and normalize this by the weighted sum of all error rates,

$$X_i = \frac{p_i \frac{\partial E(p_i)}{\partial p_i}}{\sum_i p_i \frac{\partial E(p_i)}{\partial p_i}}. \tag{C7}$$

We see that readout error dominates the total error rate for $n = 1$, while the two-qubit gate error contribution increases with n and represents 38 % of the error for $n = 3$ (see Table II). The dependence on readout error can

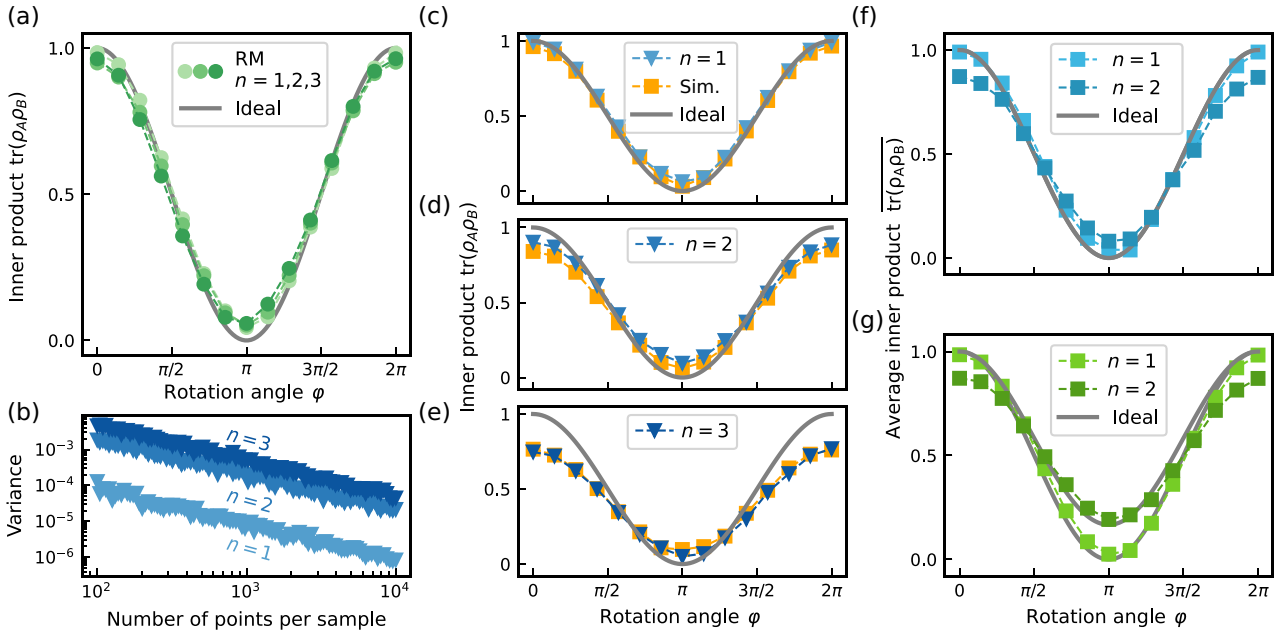


FIG. 7. (a) The inner product between $\frac{1}{\sqrt{2}}\left(|0\rangle^{\otimes n}+|1\rangle^{\otimes n}\right)$ and $\frac{1}{\sqrt{2}}\left(|0\rangle^{\otimes n}+e^{i\varphi}|1\rangle^{\otimes n}\right)$, vs φ for $n=1,2,3$ qubits, estimated using classical correlations between randomized measurements (see Appendix D). (b) The calculated variance in the inner product for $n\in\{1,2,3\}$ qubits, estimated using bootstrapping from a Bell-basis measurement data set. (c)–(e) Simulations of the Bell-basis measurement circuit presented in Fig. 3, compared to the data in Figs. 4(c) and 4(d). The error model is described in Appendix C. (f),(g) The unitary fidelity estimated using Bell-basis measurements. The unitaries to prepare the states $\frac{1}{\sqrt{2}}\left(|0\rangle^{\otimes n}+|1\rangle^{\otimes n}\right)$ and $\frac{1}{\sqrt{2}}\left(|0\rangle^{\otimes n}+e^{i\varphi}|1\rangle^{\otimes n}\right)$ from $|0\rangle$ are applied to the left and right modules, respectively, starting from all possible combinations of the cardinal states $\{|0\rangle,|1\rangle,|+\rangle,|-\rangle,|i\rangle,|-i\rangle\}$. The inner product for each initial state is calculated, and averaged over the computational states [blue curves in (f)] and cardinal states [green curves in (g)], for one and two qubits per module.

be explained by the postprocessing procedure for Bell-basis measurements, which uses the parity of the bit string resulting from a bit-wise AND operation between the measurement results on each module. A single bit flip due to a readout error leads to a flip of the parity. When these parity values are averaged for the trace overlap, these individual bit flips contribute significantly to the error.

APPENDIX D: RANDOMIZED MEASUREMENTS

As described in Sec. III, we estimate the inner product between an n-qubit $|\mathrm{GHZ}\rangle_n^{(0)}$ state on one module and an n-qubit $|\mathrm{GHZ}\rangle_n^{(\varphi)}$ state on another module using quantum state tomography. Using the theoretical frameworks of classical shadows [98] and randomized measurements (RMs) [29,73], the experimental resources required for cross-platform verification can be reduced compared to those required for full quantum state tomography. We demonstrate this with two identically prepared $|\mathrm{GHZ}\rangle_n^{(0)}$ states in Fig. 4(e) (Sec. IV).

TABLE II. The error budget for Bell-basis measurements, with the proportion of total errors that come from readout, single-qubit gates, and two-qubit gates, for experiments involving $|\mathrm{GHZ}\rangle_n^{(0)}$ states with $n\in\{1,2,3\}$ qubits. The error in the calculated percentages is less than 0.2.

	Qubits per module, n		
Error type	1	2	3
Measurement (%)	56.43	52.44	48.23
Single-qubit gates (%)	19.14	13.85	13.46
Two-qubit gates (%)	24.43	33.71	38.31

We discuss the protocol introduced in Ref. [29], in which the overlap $\mathrm{tr}\,(\rho_A\rho_B)$ is estimated from the second-order cross-correlations between measurements of the n-qubit states ρ_A and ρ_B. After state preparation, the same random unitary U is applied to both states, and they are measured in the computational basis, resulting in two bit strings of length n, s and s'. Repeating this for many unitaries, the inner product is estimated using the equation

$$\mathrm{tr}\,(\rho_A\rho_B)=2^n\sum_{s,s'}(-2)^{-D[s,s']}\overline{P_U^{(A)}(s)P_U^{(B)}(s')}, \tag{D1}$$

where $D[s,s']$ is the Hamming distance between s and s', $P_U^{(i)}(s)=\mathrm{tr}\left(U\rho_i U^\dagger|s\rangle\langle s|\right)$, and the overline denotes the average over the chosen unitaries U, as in Ref. [40].

This approach scales more favorably than quantum state tomography, with a required number of experimental repetitions $N \sim 2^{bn}$ with $b \lesssim 1$, rather than $b \geq 2$ as for quantum state tomography [73]. The exact value of b depends on the states compared and unitaries chosen. Typically, scaling is improved using unitaries selected with a greedy algorithm [40], which selects the next unitary to minimize a cost function based on the trace distance between the new unitary and the previously selected unitaries.

We analyze the phase-sweep data presented in Figs. 4(a) and 4(b) using randomized measurements. From the bases used in the quantum state tomography measurements, we select 3^n positive measurement bases using a greedy algorithm [40]. We implement this algorithm by choosing the first unitary U_1 randomly, then choose each subsequent unitary by minimizing the cost function

$$\mathcal{C}\left(\mathcal{B}, U_i\right) = -\sum_{U \in \mathcal{B}} d\left(U, U_i\right), \tag{D2}$$

where $\mathcal{B}$ is the set of previously chosen unitaries and $d(U, U_i)$ is the distance between two unitaries, defined as

$$d\left(U, U_i\right) = \sqrt{2 - |\operatorname{tr}(U^\dagger U_i)|}. \tag{D3}$$

We choose 3^n as a balance between sample efficiency and the variance of the resulting inner product. We estimate the inner product using Eq. (D1).

The estimated inner product is close to one for nominally identical states with zero phase, and close to zero for nominally orthogonal states, as expected. The resulting data are presented in Fig. 7 in Appendix E. These data agree well with the quantum state tomography data in Figs. 4(a) and 4(b).

APPENDIX E: UNITARY FIDELITY ESTIMATION

In Sec. III B, we have discussed how Bell-basis measurements can be used to estimate the inner product between two quantum states. Given the purities of the states, this allows the fidelity between them to be determined via Eq. (1). This can be straightforwardly extended to estimate process fidelities by averaging over the outcomes for different initial states [31], where the process fidelity is defined as [99]

$$\mathcal{F}_p = \frac{\operatorname{tr}\left[U_A^\dagger U_B\right]}{d^2}, \tag{E1}$$

where U_A (U_B) is the unitary operation performed on module $A(B)$. Note that in many practical scenarios, where one is interested in the process fidelity of a target unitary with respect to its noisy implementation, there exist various efficient methods to estimate the process fidelity, such as direct fidelity estimation [81] and randomized-benchmarking techniques [100–102].

To faithfully estimate the process fidelity between two unitary quantum operations U_A and U_B, one may evaluate the fidelity over an ensemble of input states. A common and effective method is to use states generated by a unitary 2-design [101,103], which approximates the statistical properties of the Haar measure. In practice, such a 2-design can be implemented by applying local random unitaries from the Clifford group to randomly selected pairs of qubits [104].

Specifically, we choose K unitaries $\{U_k\}_{k=1}^K$ that form a unitary 2-design. These unitaries generate K initial states $|k\rangle = U_k|0\rangle$ from the ground state $|0\rangle$. The average fidelity is then computed as

$$\mathcal{F}_{av}\left(U_A, U_B\right) = \frac{1}{K}\sum_{k=1}^{K}\left|\langle k|\, U_A^\dagger U_B\, |k\rangle\right|^2. \tag{E2}$$

This average fidelity relates to the process fidelity $\mathcal{F}_p$ as [105,106]

$$\mathcal{F}_p\left(U_A, U_B\right) = \frac{(d+1)\mathcal{F}_{av}\left(U_A, U_B\right) - 1}{d} \tag{E3}$$

for a Hilbert space of dimension d.

For one-qubit unitaries, the state-preparation unitaries for the cardinal states $\{|0\rangle, |1\rangle, |+\rangle, |-\rangle, |i\rangle, |-i\rangle\}$, from the ground state $|0\rangle$, form a 2-design. For higher-dimensional unitaries, preparing the necessary initial states requires a significant number of two-qubit gates, and would hence dominate the error of our Bell-basis measurement protocol. Thus, as an alternative method that does not yield the process fidelity but a metric that can be more realistically obtained on current hardware, we investigate computational basis sampling [31]. Averaging over outcomes using computational basis states yields an estimate of

$$\mathcal{F}_{sq} = \frac{1}{d}\sum_{p \in \{0,1\}^n}\left|\langle p|\, U_A^\dagger U_B\, |p\rangle\right|^2. \tag{E4}$$

While this measure is basis dependent, in contrast to the process fidelity, we can efficiently obtain it in our experiment. We consider the $|\mathrm{GHZ}\rangle_n^{(\varphi)}$ preparation unitary presented in Fig. 3, for one- and two-qubit states. Before applying the state-preparation circuit, we prepare a product state of single-qubit computational or cardinal states on each module, with the same single-qubit state on the corresponding qubits of each module. We note that for two-qubit unitaries, parallel single-qubit Clifford circuits without entangling gates do not form a 2-design, and hence the average inner product that we estimate is not related to a true process fidelity.

After applying the Bell-basis measurement circuit and estimating the inner product between the final states (using 10^5 repetitions), we average over all permutations of initial states, resulting in an average inner product. As before, we apply an additional phase φ during the application of one of the unitaries, which we vary over an entire period.

We observe a cosinusoidal variation in average inner product with the phase on one state, with reduced maximal overlap for two-qubit unitaries compared to single-qubit unitaries. We additionally observe a rightward shift in the curves, which we attribute to spectator errors [72]. These are more prevalent in the case of process fidelities, since spectator qubits are more likely to be in the excited state. We present this in Figs. 7(f) and 7(g), alongside the expected theory curve calculated using noiseless simulation. Note that we present the average inner product, which would need to be normalized by the state purity to estimate process fidelity.

[1] J. Watrous, Quantum Computational Complexity, in *Encyclopedia of Complexity and Systems Science*, edited by R. Meyers (Springer, New York, NY, USA, 2009).

[2] S. Aaronson, *Quantum Computing Since Democritus* (Cambridge University Press, Cambridge, UK, 2013).

[3] M. A. Nielsen and I. L. Chuang, *Quantum Computation and Quantum Information* (Cambridge University Press, New York, 2010), 10th Anniversary ed.

[4] K. Dalton, C. K. Long, Y. S. Yordanov, C. G. Smith, C. H. W. Barnes, N. Mertig, and D. R. M. Arvidsson-Shukur, Quantifying the effect of gate errors on variational quantum eigensolvers for quantum chemistry, npj Quantum Inf. **10**, 18 (2024).

[5] C. Gidney, How to factor 2048 bit RSA integers with less than a million noisy qubits, ArXiv:2505.15917.

[6] A. M. Dalzell, S. McArdle, M. Berta, P. Bienias, and C-F. Chen, *Quantum Algorithms: A Survey of Applications and End-to-End Complexities* (Cambridge University Press, Cambridge, UK, 2025).

[7] J. Preskill, Beyond NISQ: The megaquop machine, ACM Trans. Quantum Comput. **6**, 1 (2025).

[8] D. Awschalom, *et al.*, Development of quantum interconnects (QuICs) for next-generation information technologies, PRX Quantum **2**, 017002 (2021).

[9] S. Bravyi, O. Dial, J. M. Gambetta, D. Gil, and Z. Nazario, The future of quantum computing with superconducting qubits, J. Appl. Phys. **132**, 160902 (2022).

[10] A. Gold, J. P. Paquette, A. Stockklauser, M. J. Reagor, M. S. Alam, A. Bestwick, N. Didier, A. Nersisyan, F. Oruc, A. Razavi, B. Scharmann, E. A. Sete, B. Sur, D. Venturelli, C. J. Winkleblack, F. Wudarski, M. Harburn, and C. Rigetti, Entanglement across separate silicon dies in a modular superconducting qubit device, npj Quantum Inf. **7**, 142 (2021).

[11] M. Field, A. Q. Chen, B. Scharmann, E. A. Sete, F. Oruc, K. Vu, V. Kosenko, J. Y. Mutus, S. Poletto, and A. Bestwick, Modular superconducting-qubit architecture with a multichip tunable coupler, Phys. Rev. Appl. **21**, 054063 (2024).

[12] X. Wu, H. Yan, G. Andersson, A. Anferov, M.-H. Chou, C.-R. Conner, J. Grebel, Y. J. Joshi, S. Li, J. M. Miller, R. G. Povey, H. Qiao, and A. N. Cleland, Modular quantum processor with an all-to-all reconfigurable router, Phys. Rev. X **14**, 041030 (2024).

[13] L. D. Burkhart, J. D. Teoh, Y. Zhang, C. J. Axline, L. Frunzio, M. H. Devoret, L. Jiang, S. M. Girvin, and R. J. Schoelkopf, Error-detected state transfer and entanglement in a superconducting quantum network, PRX Quantum **2**, 030321 (2021).

[14] J. Niu, *et al.*, Low-loss interconnects for modular superconducting quantum processors, Nat. Electron. **6**, 235 (2023).

[15] P. Magnard, S. Storz, P. Kurpiers, J. Schär, F. Marxer, J. Lütolf, T. Walter, J.-C. Besse, M. Gabureac, K. Reuer, A. Akin, B. Royer, A. Blais, and A. Wallraff, Microwave quantum link between superconducting circuits housed in spatially separated cryogenic systems, Phys. Rev. Lett. **125**, 260502 (2020).

[16] S. Storz, *et al.*, Loophole-free Bell inequality violation with superconducting circuits, Nature **617**, 265 (2023).

[17] R. W. Andrews, R. W. Peterson, T. P. Purdy, K. Cicak, R. W. Simmonds, C. A. Regal, and K. W. Lehnert, Bidirectional and efficient conversion between microwave and optical light, Nat. Phys. **10**, 321 (2014).

[18] M. Mirhosseini, A. Sipahigil, M. Kalaee, and O. Painter, Superconducting qubit to optical photon transduction, Nature **588**, 599 (2020).

[19] X. Han, W. Fu, C.-L. Zou, L. Jiang, and H. X. Tang, Microwave-optical quantum frequency conversion, Optica **8**, 1050 (2021).

[20] R. Sahu, W. Hease, A. Rueda, G. Arnold, L. Qiu, and J. M. Fink, Quantum-enabled operation of a microwave-optical interface, Nat. Commun. **13**, 1276 (2022).

[21] J. Ang, *et al.*, ARQUIN: Architectures for multinode superconducting quantum computers, ACM Trans. Quantum Comput. **5**, 1 (2024).

[22] E. Magesan, J. M. Gambetta, B. R. Johnson, C. A. Ryan, J. M. Chow, S. T. Merkel, M. P. da Silva, G. A. Keefe, M. B. Rothwell, T. A. Ohki, M. B. Ketchen, and M. Steffen, Efficient measurement of quantum gate error by interleaved randomized benchmarking, Phys. Rev. Lett. **109**, 080505 (2012).

[23] E. Magesan, J. M. Gambetta, and J. Emerson, Characterizing quantum gates via randomized benchmarking, Phys. Rev. A **85**, 042311 (2012).

[24] K. Heya, T. Phung, M. Malekakhlagh, R. Steiner, M. Turchetti, W. Shanks, J. Mamin, W. S. Lu, Y. Kandel, N. Sundaresan, and J. Orcutt, Randomized benchmarking of a remote cnot gate via a meter-scale microwave link, Phys. Rev. Lett. **135**, 200801 (2025).

[25] A. Hashim, L. B. Nguyen, N. Goss, B. Marinelli, R. K. Naik, T. Chistolini, J. Hines, J.P. Marceaux, Y. Kim, P. Gokhale, T. Tomesh, S. Chen, L. Jiang, S. Ferracin, K. Rudinger, T. Proctor, K. C. Young, I. Siddiqi, and R. Blume-Kohout, Practical introduction to benchmarking and characterization of quantum computers, PRX Quantum **6**, 030202 (2025).

[26] A. W. Cross, L. S. Bishop, S. Sheldon, P. D. Nation, and J. M. Gambetta, Validating quantum computers using randomized model circuits, Phys. Rev. A **100**, 032328 (2019).

[27] T. Proctor, S. Seritan, K. Rudinger, E. Nielsen, R. Blume-Kohout, and K. Young, Scalable randomized benchmarking of quantum computers using mirror circuits, Phys. Rev. Lett. **129**, 150502 (2022).

[28] T. Proctor, K. Young, A. D. Baczewski, and R. Blume-Kohout, Benchmarking quantum computers, Nat. Rev. Phys. **7**, 105 (2025).

[29] A. Elben, B. Vermersch, R. van Bijnen, C. Kokail, T. Brydges, C. Maier, M. K. Joshi, R. Blatt, C. F. Roos, and P. Zoller, Cross-platform verification of intermediate scale quantum devices, Phys. Rev. Lett. **124**, 010504 (2020).

[30] A. Anshu, Z. Landau, and Y. Liu, in *Proceedings of the 54th Annual ACM SIGACT Symposium on Theory of Computing, STOC '22* (ACM, New York, NY, USA, 2022), p. 44.

[31] J. Knörzer, D. Malz, and J. I. Cirac, Cross-platform verification in quantum networks, Phys. Rev. A **107**, 062424 (2023).

[32] J. Denzler, S. Varona, T. Guaita, and J. Carrasco, Highly-entangled, highly-doped states that are efficiently cross-device verifiable, Phys. Rev. Res. **7**, 023320 (2025).

[33] M. Hinsche, M. Ioannou, S. Jerbi, L. Leone, J. Eisert, and J. Carrasco. Efficient distributed inner product estimation via Pauli sampling, PRX Quantum **6**, 030354 (2025).

[34] D. Aharonov, J. Cotler, and X.-L. Qi, Quantum algorithmic measurement, Nat. Commun. **13**, 887 (2022).

[35] H. Buhrman, R. Cleve, J. Watrous, and R. de Wolf, Quantum fingerprinting, Phys. Rev. Lett. **87**, 167902 (2001).

[36] A. K. Ekert, C. M. Alves, D. K. L. Oi, M. Horodecki, P. Horodecki, and L. C. Kwek, Direct estimations of linear and nonlinear functionals of a quantum state, Phys. Rev. Lett. **88**, 217901 (2002).

[37] J. C. Garcia-Escartin and P. Chamorro-Posada, SWAP test and Hong-Ou-Mandel effect are equivalent, Phys. Rev. A **87**, 052330 (2013).

[38] L. Cincio, Y. Subaşı, A. T. Sornborger, and P. J. Coles, Learning the quantum algorithm for state overlap, New J. Phys. **20**, 113022 (2018).

[39] B. Wu, *et al.*, State similarity in modular superconducting quantum processors with classical communications, ArXiv:2506.01657.

[40] D. Zhu, Z. Cian, C. Noel, A. Risinger, D. Biswas, L. Egan, Y. Zhu, A. M. Green, C. H. Alderete, N. H. Nguyen, Q. Wang, A. Maksymov, Y. Nam, M. Cetina, N. M. Linke, M. Hafezi, and C. Monroe, Cross-platform comparison of arbitrary quantum computations, Nat. Commun. **13**, 1 (2022).

[41] C. Zheng, X. Yu, and K. Wang, Cross-platform comparison of arbitrary quantum processes, npj Quantum Inf. **10**, 4 (2024).

[42] A. J. Daley, H. Pichler, J. Schachenmayer, and P. Zoller, Measuring entanglement growth in quench dynamics of bosons in an optical lattice, Phys. Rev. Lett. **109**, 020505 (2012).

[43] R. Islam, R. Ma, P. M. Preiss, M. Eric Tai, A. Lukin, M. Rispoli, and M. Greiner, Measuring entanglement entropy in a quantum many-body system, Nature **528**, 77 (2015).

[44] D. Bluvstein, H. Levine, G. Semeghini, T. T. Wang, S. Ebadi, M. Kalinowski, A. Keesling, N. Maskara, H. Pichler, M. Greiner, V. Vuletić, and M. D. Lukin, A quantum processor based on coherent transport of entangled atom arrays, Nature **604**, 451 (2022).

[45] A. H. Karamlou, I. T. Rosen, S. E. Muschinske, C. N. Barrett, A. Di Paolo, L. Ding, P. M. Harrington, M. Hays, R. Das, D. K. Kim, B. M. Niedzielski, M. Schuldt, K. Serniak, M. E. Schwartz, J. L. Yoder, S. Gustavsson, Y. Yanay, J. A. Grover, and W. D. Oliver, Probing entanglement in a 2D hard-core Bose-Hubbard lattice, Nature **629**, 561 (2024).

[46] S. Kosen, H. X. Li, M. Rommel, R. Rehammar, M. Caputo, L. Grönberg, J. Fernández-Pendás, A. Kockum, J. Biznárová, L. Chen, C. Križan, A. Nylander, A. Osman, A. Roudsari, D. Shiri, G. Tancredi, J. Govenius, and J. Bylander, Signal crosstalk in a flip-chip quantum processor, PRX Quantum **5**, 030350 (2024).

[47] K. N. Smith, G. S. Ravi, J. M. Baker, and F. T. Chong, in *Proceedings of the 55th Annual IEEE/ACM International Symposium on Microarchitecture, MICRO '22* (IEEE Press, Chicago, IL, USA, 2023) p. 1092.

[48] Y. Kim, A. Eddins, S. Anand, K. X. Wei, E. van den Berg, S. Rosenblatt, H. Nayfeh, Y. Wu, M. Zaletel, K. Temme, and A. Kandala, Evidence for the utility of quantum computing before fault tolerance, Nature **618**, 500 (2023).

[49] R. Acharya, *et al.*, Quantum error correction below the surface code threshold, Nature **638**, 920 (2025).

[50] D. Gao, *et al.*, Establishing a new benchmark in quantum computational advantage with 105-qubit Zuchongzhi 3.0 processor, Phys. Rev. Lett. **134**, 090601 (2025).

[51] G. J. Norris, K. Dalton, D. C. Zanuz, A. Rommens, A. Flasby, M. B. Panah, F. Swiadek, C. Scarato, C. Hellings, J-C. Besse, and A. Wallraff, Performance characterization of a multi-module quantum processor with static inter-chip couplers, ArXiv:2503.12603.

[52] S. Ihssen, S. Geisert, G. Jauma, P. Winkel, M. Spiecker, N. Zapata, N. Gosling, P. Paluch, M. Pino, T. Reisinger, W. Wernsdorfer, J. J. Garcia-Ripoll, and I. M. Pop, Low crosstalk modular flip-chip architecture for coupled superconducting qubits, Appl. Phys. Lett. **126**, 134003 (2025).

[53] F. W. Strauch, P. R. Johnson, A. J. Dragt, C. J. Lobb, J. R. Anderson, and F. C. Wellstood, Quantum logic gates for coupled superconducting phase qubits, Phys. Rev. Lett. **91**, 167005 (2003).

[54] L. DiCarlo, J. M. Chow, J. M. Gambetta, L. S. Bishop, B. R. Johnson, D. I. Schuster, J. Majer, A. Blais, L. Frunzio, S. M. Girvin, and R. J. Schoelkopf, Demonstration of two-qubit algorithms with a superconducting quantum processor, Nature **460**, 240 (2009).

[55] C. Hellings, N. Lacroix, A. Remm, R. Boell, J. Herrmann, S. Lazar, S. Krinner, F. Swiadek, C. Andersen, C. Eichler, and A. Wallraff, Calibrating magnetic flux control in superconducting circuits by compensating distortions on timescales from nanoseconds up to tens of microseconds, Phys. Rev. Res. **7**, 043142 (2025).

[56] T. Walter, P. Kurpiers, S. Gasparinetti, P. Magnard, A. Potočnik, Y. Salathé, M. Pechal, M. Mondal, M. Oppliger, C. Eichler, and A. Wallraff, Rapid high-fidelity single-shot

dispersive readout of superconducting qubits, Phys. Rev. Appl. **7**, 054020 (2017).

[57] J. Heinsoo, C. K. Andersen, A. Remm, S. Krinner, T. Walter, Y. Salathé, S. Gasparinetti, J.-C. Besse, A. Potočnik, A. Wallraff, and C. Eichler, Rapid high-fidelity multiplexed readout of superconducting qubits, Phys. Rev. Appl. **10**, 034040 (2018).

[58] G. J. Norris, L. Michaud, D. Pahl, M. Kerschbaum, C. Eichler, J.-C. Besse, and A. Wallraff, Improved parameter targeting in 3D-integrated superconducting circuits through a polymer spacer process, EPJ Quantum Technol. **11**, 5 (2024).

[59] S. Krinner, N. Lacroix, A. Remm, A. Di Paolo, E. Genois, C. Leroux, C. Hellings, S. Lazar, F. Swiadek, J. Herrmann, G. J. Norris, C. K. Andersen, M. Müller, A. Blais, C. Eichler, and A. Wallraff, Realizing repeated quantum error correction in a distance-three surface code, Nature **605**, 669 (2022).

[60] I. Besedin, M. Kerschbaum, J. Knoll, I. Hesner, L. Bödeker, L. Colmenarez, L. Hofele, L. Lacroix, C. Hellings, F. Swiadek, A. Flasby, M. B. Panah, D. C. Zanuz, M. Müller, and A. Wallraff, Realizing lattice surgery on two distance-three repetition codes with superconducting qubits, ArXiv:2501.04612.

[61] S. Kosen, *et al.*, Building blocks of a flip-chip integrated superconducting quantum processor, Quantum Sci. Technol. **7**, 035018 (2022).

[62] C. Scarato, K. Hanke, A. Remm, S. Lazar, N. Lacroix, D. Colao Zanuz, A. Flasby, A. Wallraff, and C. Hellings, Realizing a continuous set of two-qubit gates parameterized by an idle time, PRX Quantum **6**, 040317 (2025).

[63] K. C. Miao, *et al.*, Overcoming leakage in quantum error correction, Nat. Phys. **19**, 1780 (2023).

[64] N. Lacroix, L. Hofele, A. Remm, O. Benhayoune-Khadraoui, A. McDonald, R. Shillito, S. Lazar, C. Hellings, F. Swiadek, D. Colao-Zanuz, A. Flasby, M. B. Panah, M. Kerschbaum, G. J. Norris, A. Blais, A. Wallraff, and S. Krinner, Fast flux-activated leakage reduction for superconducting quantum circuits, Phys. Rev. Lett. **134**, 120601 (2025).

[65] M. Neeley, R. C. Bialczak, M. Lenander, E. Lucero, M. Mariantoni, A. D. O'Connell, D. Sank, H. Wang, M. Weides, J. Wenner, Y. Yin, T. Yamamoto, A. N. Cleland, and J. M. Martinis, Generation of three-qubit entangled states using superconducting phase qubits, Nature **467**, 570 (2010).

[66] H. Zhu, Quantum state estimation with informationally overcomplete measurements, Phys. Rev. A **90**, 012115 (2014).

[67] M. Steffen, M. Ansmann, R. C. Bialczak, N. Katz, E. Lucero, R. McDermott, M. Neeley, E. M. Weig, A. N. Cleland, and J. M. Martinis, Measurement of the entanglement of two superconducting qubits via state tomography, Science **313**, 1423 (2006).

[68] S. Arunachalam and L. Schatzki, Distributed inner product estimation with limited quantum communication, ArXiv:2410.12684.

[69] R. Jozsa, Fidelity for mixed quantum states, J. Mod. Opt. **41**, 2315 (1994).

[70] Y.-C. Liang, Y.-H. Yeh, P. E. M. F. Mendonça, R. Y. Teh, M. D Reid, and P. D Drummond, Quantum fidelity measures for mixed states, Rep. Progr. Phys. **82**, 076001 (2019).

[71] D. C. McKay, C. J. Wood, S. Sheldon, J. M. Chow, and J. M. Gambetta, Efficient *Z* gates for quantum computing, Phys. Rev. A **96**, 022330 (2017).

[72] S. Krinner, S. Lazar, A. Remm, C. K. Andersen, N. Lacroix, G. J. Norris, C. Hellings, M. Gabureac, C. Eichler, and A. Wallraff, Benchmarking coherent errors in controlled-phase gates due to spectator qubits, Phys. Rev. Appl. **14**, 024042 (2020).

[73] A. Elben, S. T. Flammia, H.-Y. Huang, R. Kueng, J. Preskill, B. Vermersch, and P. Zoller, The randomized measurement toolbox, Nat. Rev. Phys. **5**, 9 (2023).

[74] H. Häffner, W. Hänsel, C. F. Roos, J. Benhelm, D. Chekal-kar, M. Chwalla, T. Körber, U. D. Rapol, M. Riebe, P. O. Schmidt, C. Becher, O. Gühne, W. Dür, and R. Blatt, Scalable multiparticle entanglement of trapped ions, Nature **438**, 643 (2005).

[75] C. Song, K. Xu, W. Liu, C.-P. Yang, S.-B. Zheng, H. Deng, Q. Xie, K. Huang, Q. Guo, L. Zhang, P. Zhang, D. Xu, D. Zheng, X. Zhu, H. Wang, Y.-A. Chen, C.-Y. Lu, S. Han, and J.-W. Pan, 10-qubit entanglement and parallel logic operations with a superconducting circuit, Phys. Rev. Lett. **119**, 180511 (2017).

[76] D. Gross, Y.-K. Liu, S. T. Flammia, S. Becker, and J. Eisert, Quantum state tomography via compressed sensing, Phys. Rev. Lett. **105**, 150401 (2010).

[77] G. Tóth, W. Wieczorek, D. Gross, R. Krischek, C. Schwemmer, and H. Weinfurter, Permutationally invariant quantum tomography, Phys. Rev. Lett. **105**, 250403 (2010).

[78] M. Cramer, M. B. Plenio, S. T. Flammia, R. Somma, D. Gross, S. D. Bartlett, O. Landon-Cardinal, D. Poulin, and Y.-K. Liu, Efficient quantum state tomography, Nat. Commun. **1**, 149 (2010).

[79] J. Acharya, A. Dharmavarapu, Y. Liu, and N. Yu, in *Proceedings of the 57th Annual ACM Symposium on Theory of Computing (STOC '25)* (ACM, New York, NY, USA, 2025), p. 718.

[80] D. Binosi, G. Garberoglio, D. Maragnano, M. Dapor, and M. Liscidini, A tailor-made quantum state tomography approach, APL Quantum **1**, 036112 (2024).

[81] S. T. Flammia and Y. -K. Liu, Direct fidelity estimation from few Pauli measurements, Phys. Rev. Lett. **106**, 230501 (2011).

[82] S. D. Bartlett, Quantum computing: Powered by magic, Nature **510**, 345 (2014).

[83] Q. Wang and Z. Zhang, Fast quantum algorithms for trace distance estimation, IEEE Trans. Inf. Theory **70**, 2720 (2024).

[84] L. Bittel, F. A. Mele, A. A. Mele, S. Tirone, and L. Lami, Optimal estimates of trace distance between bosonic Gaussian states and applications to learning, Quantum **9**, 1769 (2025).

[85] R. Kueng and C. Ferrie, Near-optimal quantum tomography: Estimators and bounds, New J. Phys. **17**, 123013 (2015).

[86] H.-Y. Huang, R. Kueng, and J. Preskill, Information-theoretic bounds on quantum advantage in machine learning, Phys. Rev. Lett. **126**, 190505 (2021).
[87] A. Montanaro, Learning stabilizer states by bell sampling, ArXiv:1707.04012.
[88] D. Hangleiter and M. J. Gullans, Bell sampling from quantum circuits, Phys. Rev. Lett. **133**, 020601 (2024).
[89] K. Dalton, J. Knörzer, F. Hoehne, Y. Song, A. Flasby, D. C. Zanuz, M. B. Panah, I. Besedin, J.-C. Besse, A. Wallraff, Supporting data for "Resource-Efficient Cross-Platform Verification with Modular Superconducting Devices", https://doi.org/10.3929/ethz-c-000785951 (2025).
[90] J. J. Burnett, A. Bengtsson, M. Scigliuzzo, D. Niepce, M. Kudra, P. Delsing, and J. Bylander, Decoherence benchmarking of superconducting qubits, npj Quantum Inf. **5**, 54 (2019).
[91] J. Lisenfeld, A. Bilmes, and A. V. Ustinov, Enhancing the coherence of superconducting quantum bits with electric fields, npj Quantum Inf. **9**, 8 (2023).
[92] S. Krinner, S. Storz, P. Kurpiers, P. Magnard, J. Heinsoo, R. Keller, J. Lütolf, C. Eichler, and A. Wallraff, Engineering cryogenic setups for 100-qubit scale superconducting circuit systems, EPJ Quantum Technol. **6**, 2 (2019).
[93] J. Herrmann, C. Hellings, S. Lazăr, F. Pfäffli, F. Haupt, T. Thiele, D. C. Zanuz, G. J. Norris, F. Heer, C. Eichler, and A. Wallraff, Frequency up-conversion schemes for controlling superconducting qubits, ArXiv:2210.02513.
[94] C. Macklin, K. O'Brien, D. Hover, M. E. Schwartz, V. Bolkhovsky, X. Zhang, W. D. Oliver, and I. Siddiqi, A near-quantum-limited Josephson traveling-wave parametric amplifier, Science **350**, 307 (2015).
[95] C. C. Bultink, B. Tarasinski, N. Haandbæk, S. Poletto, N. Haider, D. J. Michalak, A. Bruno, and L. DiCarlo, General method for extracting the quantum efficiency of dispersive qubit readout in circuit QED, Appl. Phys. Lett. **112**, 092601 (2018).
[96] A. Javadi-Abhari, M. Treinish, K. Krsulich, C. J. Wood, J. Lishman, J. Gacon, S. Martiel, P. D. Nation, L. S. Bishop, A. W. Cross, B. R. Johnson, and J. M. Gambetta, Quantum computing with QISKIT, ArXiv:2405.08810.
[97] Z. Chen, *et al.*, Exponential suppression of bit or phase errors with cyclic error correction, Nature **595**, 383 (2021).
[98] S. Aaronson, in *Proceedings of the 50th Annual ACM SIGACT Symposium on Theory of Computing, STOC '18* (ACM, Los Angeles, CA, USA, 2018), p. 325.
[99] M. Raginsky, A fidelity measure for quantum channels, Phys. Lett. A **290**, 11 (2001).
[100] J. Emerson, R. Alicki, and K. Zyczkowski, Scalable noise estimation with random unitary operators, J. Opt. B: Quantum Semiclass. Opt. **7**, S347 (2005).
[101] C. Dankert, R. Cleve, J. Emerson, and E. Livine, Exact and approximate unitary 2-designs and their application to fidelity estimation, Phys. Rev. A **80**, 012304 (2009).
[102] A. Erhard, J. J. Wallman, L. Postler, M. Meth, R. Stricker, E. A. Martinez, P. Schindler, T. Monz, J. Emerson, and R. Blatt, Characterizing large-scale quantum computers via cycle benchmarking, Nat. Commun. **10**, 5347 (2019).
[103] D. Gross, K. Audenaert, and J. Eisert, Evenly distributed unitaries: On the structure of unitary designs, J. Math. Phys. **48**, 052104 (2007).
[104] F. G. S. L. Brandão, A. W. Harrow, and M. Horodecki, Local random quantum circuits are approximate polynomial-designs, Commun. Math. Phys. **346**, 397 (2016).
[105] M. Horodecki, P. Horodecki, and R. Horodecki, General teleportation channel, singlet fraction, and quasidistillation, Phys. Rev. A **60**, 1888 (1999).
[106] M. A. Nielsen, A simple formula for the average gate fidelity of a quantum dynamical operation, Phys. Lett. A **303**, 249 (2002).